aerospace

MDPI

Article

Data-Driven Reduced-Order Modeling for Aeroelastic Load Prediction of Rotor Blades

Nan Luo, Zhihao Yu * and Weidong Yang

National Key Laboratory of Helicopter Aeromechanics, Nanjing University of Aeronautics and Astronautics, Nanjing 210016, China
* Correspondence: zhihao@nuaa.edu.cn

Abstract

This paper proposes a data-driven model for predicting rotor fluid-structure interaction (FSI) load with efficient aeroelastic analysis. Unsteady flow-field snapshots obtained from computational fluid dynamics (CFD) simulations are first processed using Proper Orthogonal Decomposition (POD) to reduce the dimensionality of the flow data and extract the dominant modal time coefficients. Based on these reduced-order representations, the Dynamic Mode Decomposition with control (DMDc) method is used to identify a time-domain state-space model of the aerodynamic system. The identified data-driven aerodynamic model is coupled with the structural dynamic equations, which allows time-domain reconstruction and prediction of unsteady aerodynamic forces and structural loads under aeroelastic interactions. Hence, an efficient reduced-order model for aerodynamic load is established. The proposed approach is first validated using a two-dimensional airfoil subjected to different motion inputs, where the reduced-order aerodynamic predictions are compared with high-fidelity CFD results. Then, a three-dimensional sectional reduced-order model for a rotor is developed based on blade element theory, and aeroelastic coupled simulations are conducted for the SA349 rotor. The results demonstrate that the proposed method can accurately capture unsteady aerodynamic loads and aeroelastic responses, while significantly improving computational efficiency compared to high-fidelity simulations.

Keywords: rotor; data-driven; reduced-order model; unsteady aerodynamics; fluid-structure interaction; vibrator loads

1. Introduction

The unique operating characteristics of helicopter rotors result in a highly complex aerodynamic environment for the blades, in which strongly nonlinear phenomena such as blade–vortex interaction (BVI) are commonly encountered [1]. From a structural mechanics perspective, a rotor blade can be modeled as a flexible cantilever beam. When these complex, unsteady aerodynamic loads act directly on the blade and are coupled with the structural response, blade deformations—including flapping, lagging, and torsion—may be induced, resulting in structural vibrations. In severe cases, such vibrations can compromise flight stability or lead to fatigue damage of the rotor blades. Moreover, these dynamic loads are transmitted to the fuselage through the rotor hub, thereby affecting the fatigue life of the airframe, the reliable operation of onboard equipment, and the ride comfort of occupants. Consequently, the rapid and accurate prediction of structural loads on helicopter rotor blades is of critical importance.

Check for updates

Academic Editor: Ioannis Goulos

Received: 30 January 2026
Revised: 28 February 2026
Accepted: 10 March 2026
Published: 17 March 2026

Copyright: © 2026 by the authors. Licensee MDPI, Basel, Switzerland. This article is an open access article distributed under the terms and conditions of the Creative Commons Attribution (CC BY) license.

In recent decades, significant progress has been achieved in aeroelastic modeling methodologies for rotorcraft. Traditional approaches are primarily physics-based and typically rely on the combination of structural beam theories and simplified aerodynamic models. From the structural modeling perspective, rotor blades are commonly idealized as flexible beam structures. The Euler–Bernoulli beam formulation [2], the modified Bauchau and Hong's beam model [3], and geometrically exact beam theory [4] have been widely employed to describe the elastic deformation of rotor blades, offering reasonable computational efficiency while maintaining physical consistency. In particular, the geometrically exact beam framework utilizes the variational asymptotic method to reduce the fully three-dimensional geometrically nonlinear elasticity problem into a one-dimensional geometrically exact beam model coupled with a two-dimensional variational asymptotic cross-sectional analysis [5]. With further developments, additional refinements—such as inertia-load-based dynamic deflection modeling [6] and fully intrinsic governing equations—have been introduced to account for structural effects, including initial twist and curvature in composite rotor blades [7].

On the aerodynamic side, these structural models are typically coupled with appropriately simplified flow representations to construct unsteady aerodynamic load models based on airfoil characteristics. Common approaches include Theodorsen's unsteady aerodynamic theory [8], dynamic inflow theory [9], free-wake methods [10], and the Peters–He finite-state dynamic wake model [11], all of which enable computationally efficient time-domain analysis. While these methods are attractive in terms of efficiency and implementation simplicity, they may exhibit limitations in accurately capturing complex flow phenomena, such as flow separation and other strongly nonlinear effects. Consequently, their aerodynamic fidelity may be reduced under conditions involving pronounced unsteady nonlinear aerodynamics.

At an earlier stage, NASA [12] pioneered the application of CFD to rotor aerodynamic analysis and loosely integrated the CFD solver with the structural dynamics code CAMRAD, demonstrating encouraging performance in subsequent validations. Building upon these efforts, the University of Maryland [13] performed coupled simulations of the SA349/2 rotor using a CFD solver integrated with the computational structural dynamics (CSD) code UMARC; however, certain limitations in convergence and accuracy were reported. With the progressive maturation of Reynolds-averaged Navier–Stokes (RANS)-based CFD techniques [14], aerodynamic predictions have achieved substantially improved accuracy and broader applicability compared with earlier reduced-fidelity models. As a result, coupled CFD/CSD approaches have been increasingly applied to forward-flight simulations of the UH-60A rotor [15,16] and its scaled HART II model [17]. It is widely recognized that aerodynamic load prediction remains one of the dominant sources of modeling uncertainty and computational cost in rotor aeroelastic analysis.

At present, the accurate characterization of complex unsteady rotor flows still largely relies on high-fidelity simulations, whose substantial computational cost poses challenges for control-law development and multidisciplinary design optimization of rotor blades. Moreover, in rotor aeroelastic analysis, the aerodynamic module often constitutes one of the primary sources of modeling uncertainty and computational expense due to the strongly nonlinear and highly unsteady nature of rotor flows. Therefore, improving the efficiency and fidelity of aerodynamic prediction remains a central issue in practical aeroelastic simulations. In this context, the development of ROMs that can accurately capture unsteady flow physics while significantly reducing computational cost has emerged as an important research focus.

In recent years, full-order flow-field decomposition methods based on feature extraction have attracted considerable attention [18,19]. These approaches aim to achieve

a high-fidelity representation of the flow field while retaining the dominant dynamical characteristics of the system. Among them, modal decomposition has been extensively developed as a representative reduced-order modeling (ROM) technique. The core idea is to extract low-dimensional modal bases from flow-field snapshots collected over a finite time interval using decomposition algorithms, and to reconstruct high-dimensional unsteady flow fields through linear combinations of these modes, thereby accurately describing the temporal evolution of flow variables. Representative examples include Proper Orthogonal Decomposition (POD) [20] and Dynamic Mode Decomposition (DMD) [19].

POD was first introduced into fluid mechanics by Lumley [21] for the analysis of turbulent flows. It was subsequently applied to the dimensional reduction in CFD models based on the Euler equations and to reduced-order aerodynamic modeling of two-dimensional airfoils [22]. Later studies demonstrated that unsteady flow features could be effectively represented through linear combinations of POD modes following global flow-field decomposition [23]. At present, POD has been widely applied to flow past circular cylinders [24], airfoil aerodynamics [25], and the dynamic analysis of wings.

DMD, proposed by Schmid [19], is a data-driven method for the analysis of dynamical systems. Each DMD mode is associated with a distinct frequency and growth (or decay) rate, and the corresponding eigenvalues directly characterize the stability and growth behavior of the flow. Building upon the standard DMD framework, Proctor et al. [26] integrated control theory and proposed the Dynamic Mode Decomposition with Control (DMDc) method, which extends DMD by incorporating system inputs and enables the simultaneous identification of both system and control matrices. DMDc has since been successfully applied in studies of unsteady aerodynamic modeling [27,28] and aeroelastic response prediction [29,30].

This study proposes a data-driven ROM approach in which high-fidelity full-order CFD simulations are first performed, followed by POD-based dimensionality reduction to extract the dominant flow features. Unlike conventional POD-based ROMs that primarily focus on modal reconstruction or regression-based surrogate modeling, the present framework directly identifies the input–output dynamical relationship of sectional unsteady aerodynamic loads within the reduced subspace through DMDc-based state-space identification. The resulting reduced representation is then used to construct an unsteady aerodynamic model with improved dynamical consistency. The identified aerodynamic model is further coupled with a CSD model based on a geometrically exact beam formulation derived from Hamilton's principle. In addition, a loosely coupled aeroelastic strategy is adopted, which helps maintain satisfactory prediction accuracy while significantly reducing the overall computational cost [31,32].

2. Data-Driven ROM Methods and Numerical Simulation

2.1. Proper Orthogonal Decomposition

During the flow-field simulations, sequences of unsteady aerodynamic force snapshots are sampled from the flow field to form the basis of the data-driven modeling process. These snapshots are assembled into a snapshot matrix, in which each column represents the aerodynamic load distribution at a given time instant. POD is then applied to the snapshot matrix to extract a set of dominant spatial modes, allowing for the projection of high-dimensional aerodynamic data onto a low-dimensional subspace. The corresponding temporal coefficients characterize the time evolution of the unsteady aerodynamic loads and serve as the reduced-order representation for subsequent modeling.

$$F = \begin{bmatrix} f_{1,1} & f_{1,2} & \cdots & f_{1,m} \\ f_{2,1} & f_{2,1} & \cdots & f_{2,m} \\ \vdots & \vdots & \ddots & \vdots \\ f_{j,1} & f_{j,2} & \cdots & f_{j,m} \end{bmatrix} = \begin{bmatrix} F_1 & F_2 & \cdots & F_m \end{bmatrix} \quad (1)$$

In the above formulation, F_i denotes the aerodynamic force snapshot obtained from the flow-field simulations. The snapshots are sampled from the continuous aerodynamic force history $F(t)$ at a fixed time interval Δt, and can be expressed as

$$F_i = F(i \times \Delta t) \quad (2)$$

To isolate the unsteady aerodynamic response, the steady component is removed from the aerodynamic force data.

$$F' = F - \overline{F} = \sum_{j=1}^{n} A_j \phi_j \quad (3)$$

In Equation (3), F denotes the total aerodynamic force obtained from the flow-field simulations. The steady component $\overline{F}$ is obtained by time averaging, and the remaining fluctuating part F' represents the unsteady aerodynamic contribution. The unsteady aerodynamic force is further expressed as a linear superposition of POD modes, where ϕ_j represents the j-th spatial mode and A_j is the corresponding temporal coefficient.

To characterize the spatial features of the unsteady aerodynamic force modes in the flow field, the POD method is employed to extract the dominant modes of the system. The snapshot matrix of the unsteady aerodynamic forces, F' is decomposed using singular value decomposition (SVD) as

$$F' = U \Sigma V^T \quad (4)$$

where $U \in R^{n \times n}$, $\Sigma \in R^{n \times m}$, and $V \in R^{m \times m}$. The matrices U and V consist of the left and right singular vectors, respectively, representing the spatial modes (mode shapes) and the temporal modes associated with the unsteady aerodynamic forces. The matrix Σ is a diagonal matrix whose diagonal entries are the singular values. The matrices U and V can be written as

$$\begin{aligned} U &= \begin{bmatrix} u_1 & u_2 & \cdots & u_n \end{bmatrix} \\ V &= \begin{bmatrix} v_1 & v_2 & \cdots & v_m \end{bmatrix} \end{aligned} \quad (5)$$

where ψ_i and v_i denote the i-th spatial mode and the corresponding temporal mode, respectively. The singular value matrix Σ is defined as

$$\Sigma = \begin{bmatrix} diag[\sigma_i]_{i \epsilon I_m} \\ 0 \end{bmatrix}, \ \sigma_1 \geq \sigma_2 \geq \cdots \geq \sigma_m \geq 0 \quad (6)$$

An energy-based truncation criterion is adopted to determine the reduced-order subspace. The singular values σ_i reflect the energy content of the corresponding modes, and the cumulative energy ratio of the first r modes is defined as

$$\eta(r) = \frac{\sum_{i=1}^{r} \sigma_i^2}{\sum_{i=1}^{m} \sigma_i^2} \quad (7)$$

The reduced-order basis is constructed by retaining the first r modes such that the cumulative energy ratio $\eta(r)$ is greater than or equal to 99%.

Therefore, the SVD of the unsteady aerodynamic snapshot matrix can be simplified as

$$F' = \begin{bmatrix} \widetilde{U} & U_{rem} \end{bmatrix} \begin{bmatrix} \widetilde{\Sigma} & 0 \\ 0 & \Sigma_{rem} \end{bmatrix} \begin{bmatrix} \widetilde{V}^T \\ V_{rem}^T \end{bmatrix} \tag{8}$$

where $\widetilde{U} \in R^{n \times r}$, $\widetilde{\Sigma} \in R^{r \times r}$, and $\widetilde{V} \in R^{m \times r}$ denote the truncated left singular vectors, singular value matrix, and right singular vectors, respectively. Figure 1 shows the overall workflow of the POD.

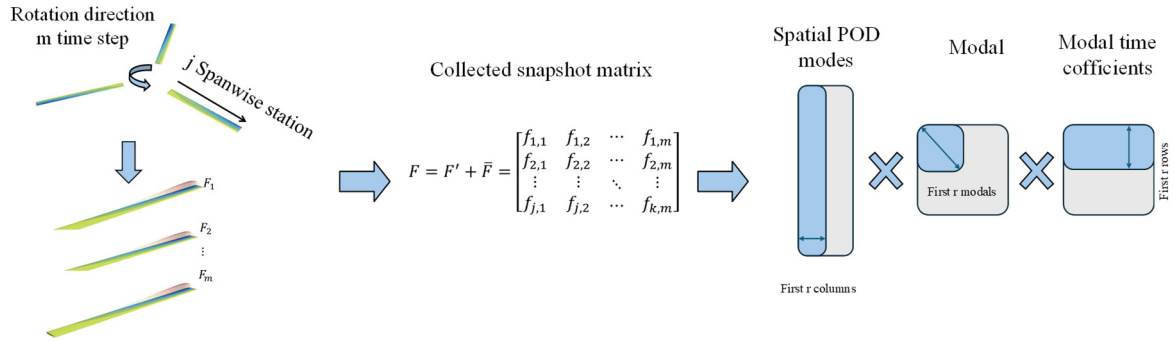


Figure 1. Schematic illustration of POD-based model reduction.

2.2. DMDc–Based State-Space Identification

The POD-based dimensionality reduction yields a low-dimensional representation of the unsteady aerodynamic forces in terms of a set of dominant spatial modes and their corresponding temporal coefficients. While POD effectively captures the energetic content of the system, it does not explicitly provide a dynamical model governing the temporal evolution of these coefficients. To address this limitation, the DMDc method is subsequently employed to identify a reduced-order state-space model that describes the time evolution of the POD modal coefficients under prescribed inputs.

The core idea of DMDc is to analyze the relationship between the system state at the next time step, X_{k+1}, and the current measured state X_k together with the control input. It is commonly assumed that this relationship can be approximated by a linear state-space model, which can be expressed as

$$X_{k+1} = AX_k + B\gamma_k \tag{9}$$

where $X_k \in R^r$ and $\varsigma_k \in R^l$ denote the state vector and the control input vector, respectively, with X_k representing the POD modal temporal coefficients in the present study. The matrices $A \in R^{r \times r}$ and $B \in R^{r \times l}$ are the system and control matrices to be identified.

In general, aerodynamic models take the structural displacement vector as the system input. To account for the time-dependent nature of the aerodynamic system, both the displacement vector and its history over a prescribed time window are considered. Accordingly, the model input is constructed in the following form:

$$\begin{aligned} \xi_k &= \begin{bmatrix} \varsigma^T(k-N) & \cdots & \varsigma^T(k-1) & \varsigma^T(k) \end{bmatrix}^T \\ \varsigma(i) &= \begin{bmatrix} M_a & \alpha(i) & \dot{\alpha}(i) & h(i) & \dot{h}(i) \end{bmatrix} \end{aligned} \tag{10}$$

where $\xi \in R^p$ denotes the structural motion displacement vector of the rotor blade model, N represents the number of delayed inputs, M_a denotes the freestream Mach number (incoming flow velocity), α and $\dot{\alpha}$ are the pitching angle and pitching angular velocity of the airfoil section, respectively, while h and $\dot{h}$ correspond to the plunging displacement

and plunging velocity. Different input delay selections influence the SVD characteristics of the augmented matrix constructed from the time coefficient snapshots and the external inputs. Typically, two or more delayed input terms are introduced to effectively represent the aerodynamic lag and memory effects inherent in unsteady aerodynamics.

The system and control matrices A and B are identified using a least-squares approach by minimizing the prediction error between the measured and reconstructed states, which can be written as

$$\begin{gathered} X_k = \begin{bmatrix} x_{N+1} & x_{N+2} & \cdots & x_{m-1} \end{bmatrix} \quad X_{k+1} = \begin{bmatrix} x_{N+2} & x_{N+3} & \cdots & x_m \end{bmatrix} \\ \gamma = \begin{bmatrix} \xi_{N+1} & \xi_{N+2} & \cdots & \xi_{m-1} \end{bmatrix} \end{gathered} \tag{11}$$

Based on the foregoing analysis, Equation (9) can be rewritten as

$$X_{k+1} = AX_k + B\varsigma_k = \begin{bmatrix} A & B \end{bmatrix} \begin{bmatrix} X_k \\ \varsigma_k \end{bmatrix} = G\Omega \tag{12}$$

All parameters to be identified are assembled in the matrix **G**, whose optimal estimate can be expressed as

$$\begin{gathered} G = X_{k+1}\Omega^{+} \\ \begin{bmatrix} A & B \end{bmatrix} = X_{k+1} \begin{bmatrix} X_k \\ \varsigma_k \end{bmatrix}^{+} \end{gathered} \tag{13}$$

The superscript $(\cdot)^{+}$ indicates the Moore–Penrose pseudoinverse. The parameter matrix is subsequently identified through the SVD of Ω.

$$\begin{bmatrix} A & B \end{bmatrix} = \begin{bmatrix} X_{k+1}\hat{V}\hat{\Sigma}^{-1}\hat{U}_1^T & X_{k+1}\hat{V}\hat{\Sigma}^{-1}\hat{U}_2^T \end{bmatrix} \tag{14}$$

Figure 2 presents the DMDc identification process. Consequently, a reduced-order time-domain dynamical model can be obtained.

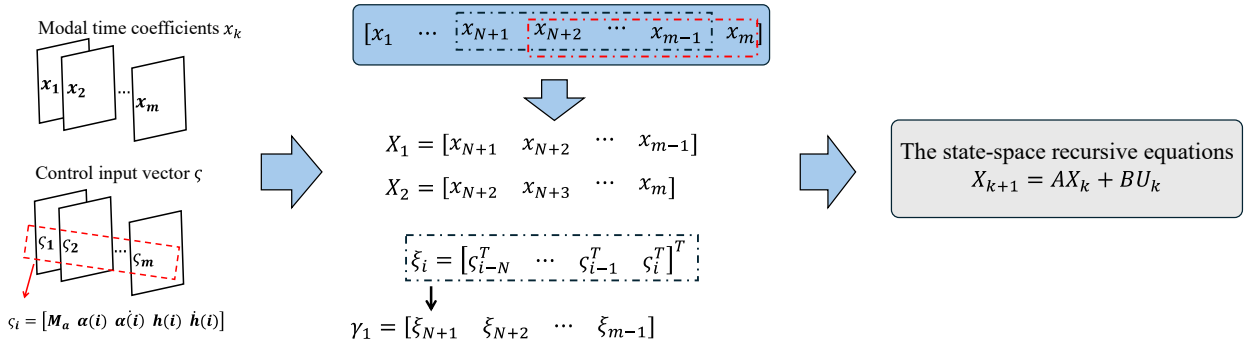


Figure 2. Schematic of the DMDc parameter identification process.

2.3. Performance Evaluation of Prediction Models

In order to quantitatively evaluate the predictive accuracy of the ROM [33], several statistical error metrics are employed, including the mean absolute error (MAE), mean squared error (MSE), root mean squared error (RMSE), and the coefficient of determination (R^2).

For the MAE, it is used to quantify the average magnitude of the differences between the predicted results and the CFD reference data, providing an intuitive measure of the overall prediction accuracy without emphasizing extreme deviations. It is defined as

$$E_{MAE} = \frac{1}{N}\sum_{i=1}^{N}\left|F_i^{CFD} - F_i^{ROM}\right| \tag{15}$$

Second, the mean squared error (MSE) and root mean squared error (RMSE) place greater emphasis on larger deviations due to the squared error term, making them more sensitive to peak discrepancies between the predicted and reference values. These metrics are therefore particularly suitable for assessing errors at higher amplitudes. They are expressed as

$$\begin{aligned} E_{MSE} &= \frac{1}{N}\sum_{i=1}^{N}\left(F_i^{CFD} - F_i^{ROM}\right)^2 \\ E_{RMSE} &= \sqrt{\frac{1}{N}\sum_{i=1}^{N}\left(F_i^{CFD} - F_i^{ROM}\right)^2} \end{aligned} \tag{16}$$

Finally, the coefficient of determination R^2 is employed to evaluate the overall goodness of fit between the ROM predictions and the CFD results, reflecting how well the reduced-order model captures the global trend of the aerodynamic response. It is given by

$$E_{R^2} = 1 - \frac{\sum_{i=1}^{N}\left(F_i^{CFD} - F^{MEA}\right)^2}{\sum_{i=1}^{N}\left(F_i^{CFD} - F_i^{ROM}\right)^2} \tag{17}$$

In Equations (15)–(17) are defined as follows, N denotes the total number of time samples used in the error evaluation; F refers to the aerodynamic coefficients under consideration, namely the lift coefficient C_l or the moment coefficient C_m, F_i^{ROM} represent the aerodynamic coefficients obtained from the CFD simulations at the i-th time step and F_i^{ROM} is prediction from the reduced-order model at the i-th time step, F^{MEA} denotes the mean value of the CFD results over all samples, which is given by

$$F^{MEA} = \frac{1}{N}\sum_{i=1}^{N} F_i^{CFD} \tag{18}$$

2.4. Computation Structural Dynamic Model

To compute the structural loads of the rotor blade, large deformation effects are considered. Based on the Green strain tensor, the strain and kinetic energy expressions of the blade are established, and the governing dynamic equations are derived via Hamilton's principle [34].

$$\delta\Pi = \int_{t_1}^{t_2}(\delta U - \delta T - \delta W)dt = 0 \tag{19}$$

where δU is the virtual variation in strain energy; δT is the virtual variation of kinetic energy; δW is the virtual work of external loads.

The variation in the kinetic energy can be written as

$$\delta T = \delta q\left(M\ddot{q} + F_{NL}\right) \tag{20}$$

Here, M denotes the mass matrix of the blade, F_{NL} represents the nonlinear force vector, and q is the generalized displacement vector, including the translational and rotational displacements in the X, Y, and Z directions.

The variation in the blade strain energy can be expressed as

$$\delta U = \delta q\int K^T HKqdx = \delta q F_U \tag{21}$$

Here, F and M denote the aerodynamic force and aerodynamic moment acting on the blade, respectively; F_U represents the generalized force induced by aerodynamic loading; and G_b is the generalized force coefficient matrix, which can be expressed as

$$G_b = \begin{bmatrix} C^{EI} & C^{EB}\tilde{R}^{EB}_{BV}L^{BI} & C^{EB}H_{EI} & 0 \\ 0 & C^{EB}L^{BI} & 0 & C^{EB}H_{EI} \end{bmatrix}^T \tag{22}$$

After solving for the structural response of the rotor blade, a hybrid computational approach is adopted in this study to evaluate the blade structural loads, as illustrated in Figure 3.

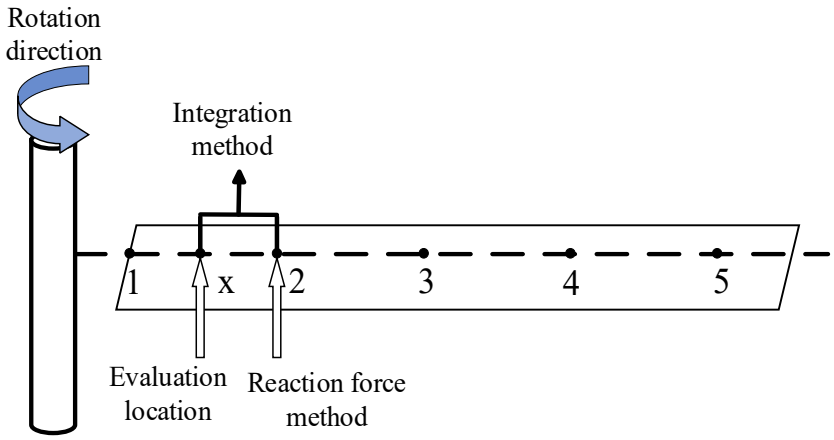


Figure 3. Load Calculation Method.

The load at the sectional location corresponding to point X can be expressed as

$$F(x) = F(x_2) + M(x_2) + \int_x^{x_2} f(x)dx \tag{23}$$

Here, $F(x_2)$ and $M(x_2)$ denote the blade shear force and bending moment at node 2, which are obtained using the reaction force method. The subsequent integral term represents the distributed load between the sectional location of point X and node 2 and is evaluated using the force integration method.

2.5. Aeroelastic Coupling Method

In order to ensure sufficient accuracy while maintaining high computational efficiency, a loosely coupled strategy is employed to realize data transfer between the flow-field and structural domains. The aerodynamic loads acting on the rotor disk, including lift, drag, and moments, are first obtained from the flow-field domain and applied to the structural solver to compute the blade response. The resulting blade deformation is then fed back into the POD–DMDc reduced-order aerodynamic model, where the aerodynamic loads are updated after each coupling iteration. Figure 4 presents the overall computational procedure of the proposed framework, and the detailed steps are summarized below.

Step 1: An initialization procedure is first performed by prescribing the blade control inputs and conducting a trim calculation. After initialization, the blade motion input parameters are determined.

Step 2: Based on the aerodynamic results obtained from CFD simulations, the parameters of the reduced-order model are identified, and a complete reduced-order aerodynamic model is constructed.

Step 3: Using the initialized motion input parameters, the sectional aerodynamic loads acting on the blade are computed.

Step 4: The aerodynamic loads obtained in Step 3 are then transferred to the structural module. With the established structural model, the radial structural response and blade deformations, including flapping and torsional deformations, are evaluated.

Step 5: The blade deformations obtained in Step 4 are taken as inputs to the aerodynamic surrogate model to predict the aerodynamic coefficients (e.g., lift and moment coefficients) for the subsequent cycle.

Step 6: While keeping the control inputs unchanged, Steps 3 through 5 are repeated until the blade structural deformation no longer varies with the iteration count, indicating convergence of the coupled solution.

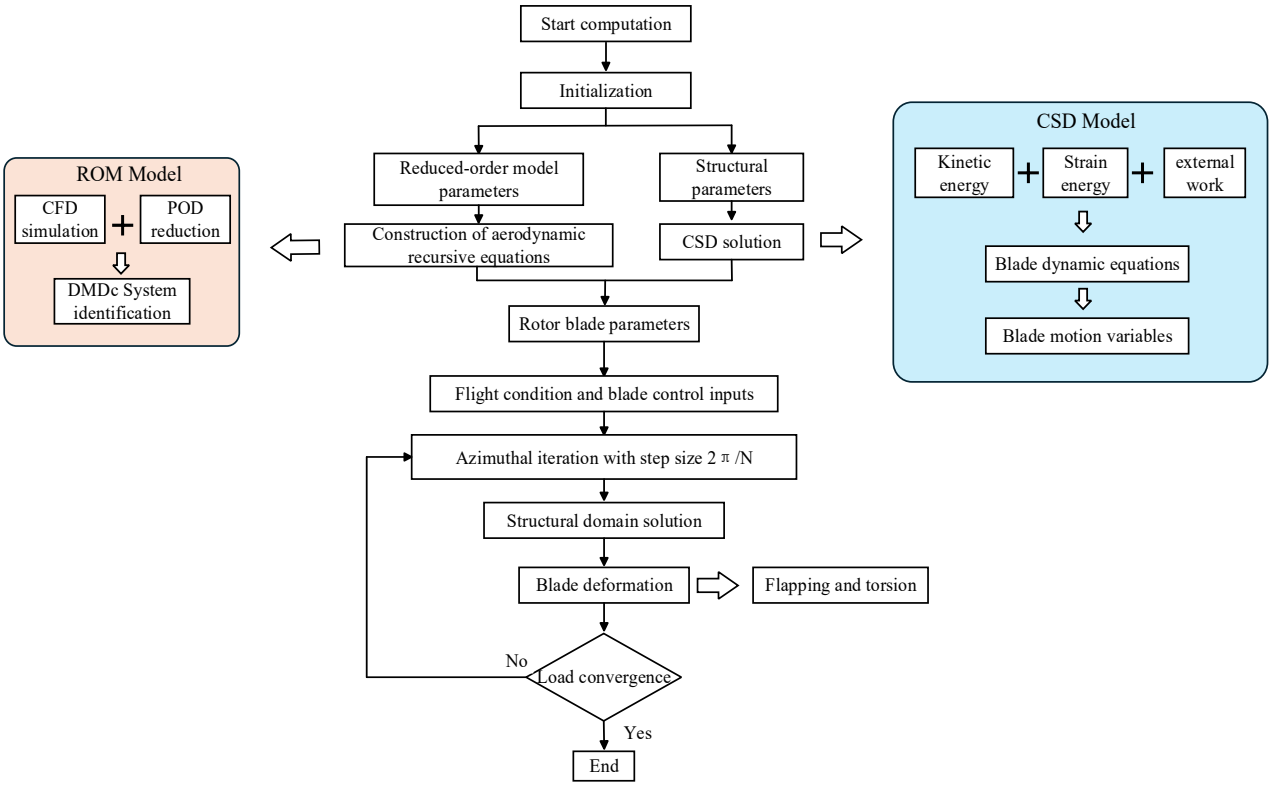


Figure 4. Aeroelastic Coupling calculation flowchart of the developed model.

3. Validation of the CFD Solver

To validate the proposed ROM model, high-fidelity CFD simulations are first performed to provide reference aerodynamic data. This section describes the CFD solver, numerical schemes, and computational setup used in the present study. The CFD solver supports both Euler and Navier–Stokes formulations with various turbulence closures; the Spalart–Allmaras (SA) model is employed in this study. To verify the computational accuracy of the CFD model, unsteady aerodynamic simulations are performed for a standard NACA0012 airfoil. The airfoil undergoes pitching motion about its quarter-chord point, and the pitching motion is described by the following equation:

$$\begin{gathered} \alpha = \alpha_0 + \alpha_1 sin(\omega t) \\ k = \frac{\omega c}{2V} \end{gathered} \tag{24}$$

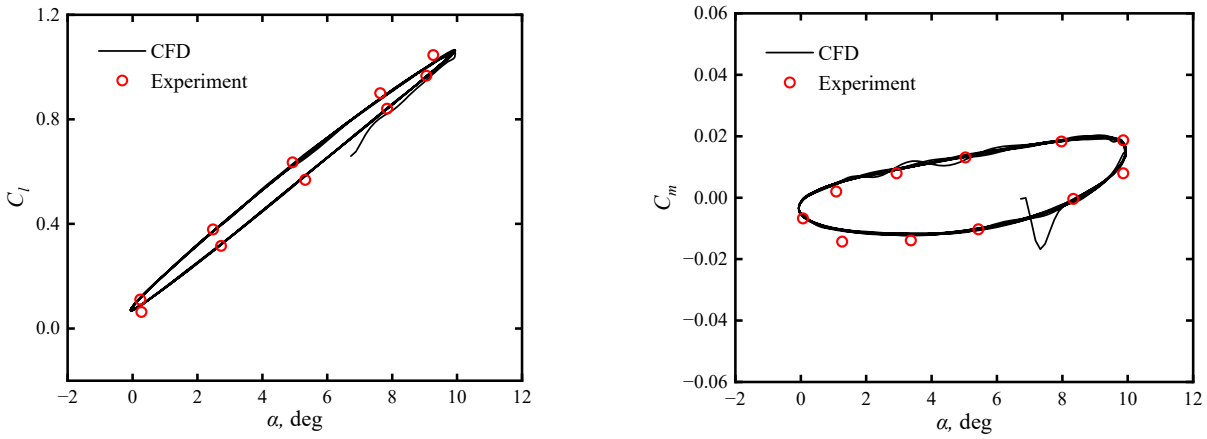
To validate the CFD solver, aerodynamic loads of the rotor blade are computed using high-fidelity CFD simulations with overset structured mesh. To accurately capture the

boundary-layer flow on the blade surface, the near-wall mesh is refined such that the dimensionless wall distance satisfies $y^+ \approx 1$. The key simulation parameters are listed in Table 1.

Table 1. Parameters of the Airfoil.

Parameters	Values
Airfoil	NACA0012
Chord Length c/m	0.61
Initial angle of attack $\alpha_0/(^\circ)$	4.94
Pitching amplitude $\alpha_1/(^\circ)$	5
Reduced frequency k	0.099
Freestream velocity V/Ma	0.301

The computed lift and pitching moment coefficients of the airfoil are compared with wind tunnel experimental data taken from Ref. [35], as shown in Figure 5. The CFD results exhibit good agreement with the reference data over the considered angle-of-attack range at a freestream Mach number of $M = 0.301$. The linear variation in the lift coefficient and the overall trend of the pitching moment coefficient are both well captured. This validation confirms the reliability of the CFD solver and provides a solid basis for subsequent ROM construction and aeroelastic coupling analyses.



(**a**) (**b**)

Figure 5. Comparison of Airfoil aerodynamic between CFD results and experimental data: (**a**) Lift coefficient C_l; (**b**) moment coefficient C_m.

4. ROM Model Studies and Discussions

To validate the proposed reduced-order aerodynamic model, a two-dimensional NACA0012 airfoil undergoing pitching and plunging motions at a Mach number of 0.301 is considered. The aerodynamic loads predicted by the ROM are compared with those obtained from direct CFD simulations for different motion amplitudes and frequencies, in order to evaluate the model's predictive accuracy and generalization capability under the same excitation conditions.

4.1. Training Excitation Signals for ROM

The stability of the identified state-space model is highly sensitive to the choice of input excitation signals. Previous studies have successfully employed various excitation strategies, including Walsh function [36], Filtered White Gaussian Noise (FWGN) [37], hybrid pulse signals [38], and multi-frequency sinusoidal excitations [39]. Such excitation

schemes are designed to more effectively capture the spatial modal characteristics of the system and to enhance the numerical stability of the DMDc.

In this study, FWGN is used as the input excitation signal. Two FWGN-based signals are generated to cover the primary ranges of motion amplitude and reduced frequency, ensuring that a wide range of spatial and temporal aerodynamic modes can be excited within a single simulation. Figure 6 shows that the reduced-frequency range goes from 0 to 0.49, and the maximum plunging displacement is less than 20% of the airfoil chord length. According to Refs. [40,41], aerodynamic nonlinearities can appear when the pitching amplitude is larger than 0.02 rad and the plunging amplitude h/b is larger than 0.3. To test the predictive ability of the ROM on data not used in training, the first 2000 time steps are used for ROM training and identification, and the last 1000 time steps are used for aerodynamic reconstruction and prediction. Separate ROMs are also built for the lift coefficient and the moment coefficient to better capture their unsteady aerodynamic responses.

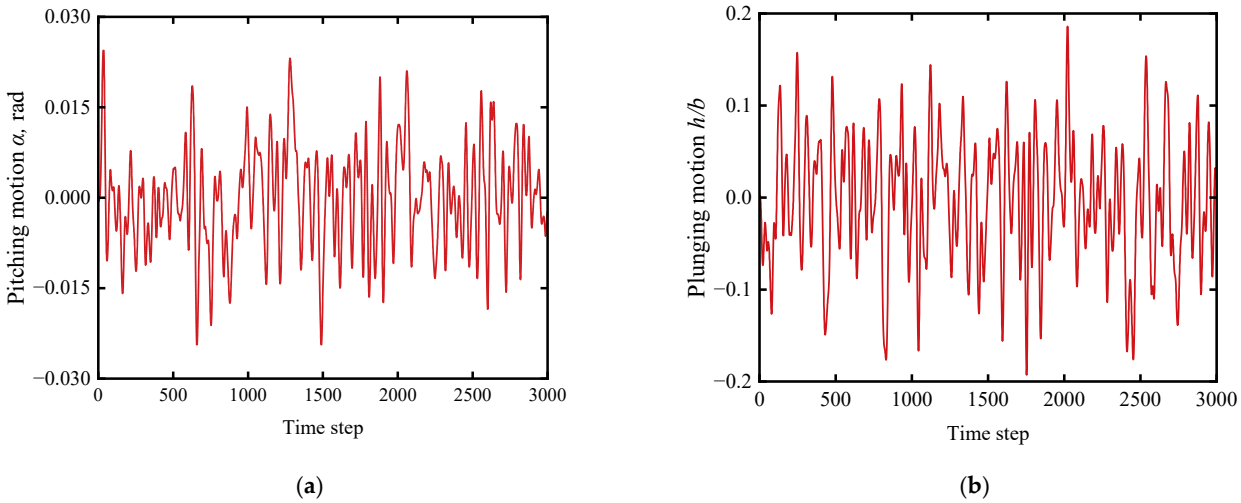


Figure 6. FWGN-based input excitation signals for reduced-order model training: (**a**) Pitching motion and (**b**) plunging motion.

The ROM is then employed to reconstruct the unsteady aerodynamic loads of the airfoil based on the prescribed input signals and the reconstructed aerodynamic responses in the frequency domain, as shown in Figure 7. ROM demonstrates good agreement with the CFD results in both the time and frequency domains during the prediction interval. The locations of the primary spectral peaks and the overall energy distribution exhibit good agreement across the investigated reduced-frequency range. While minor discrepancies are observed at higher reduced frequencies (The maximum relative error is approximately 6.82%), these differences are primarily associated with the truncation of higher-order POD modes and the linear approximation adopted in the modeling framework, in which certain nonlinear aerodynamic effects are not explicitly represented. Overall, the ROM demonstrates satisfactory capability in capturing the essential unsteady aerodynamic characteristics in both the time and frequency domains.

4.2. ROM Prediction Under Independent Pitching and Plunging Motions

Following the validation under broadband FWGN excitation, separate input signals are constructed for the pitching and plunging motions of the airfoil to further evaluate the predictive performance of the established ROM. Based on the identified ROM, the aerodynamic responses corresponding to each individual motion are predicted and subse-

quently compared with the reference CFD results, allowing for a detailed assessment of the model's capability.

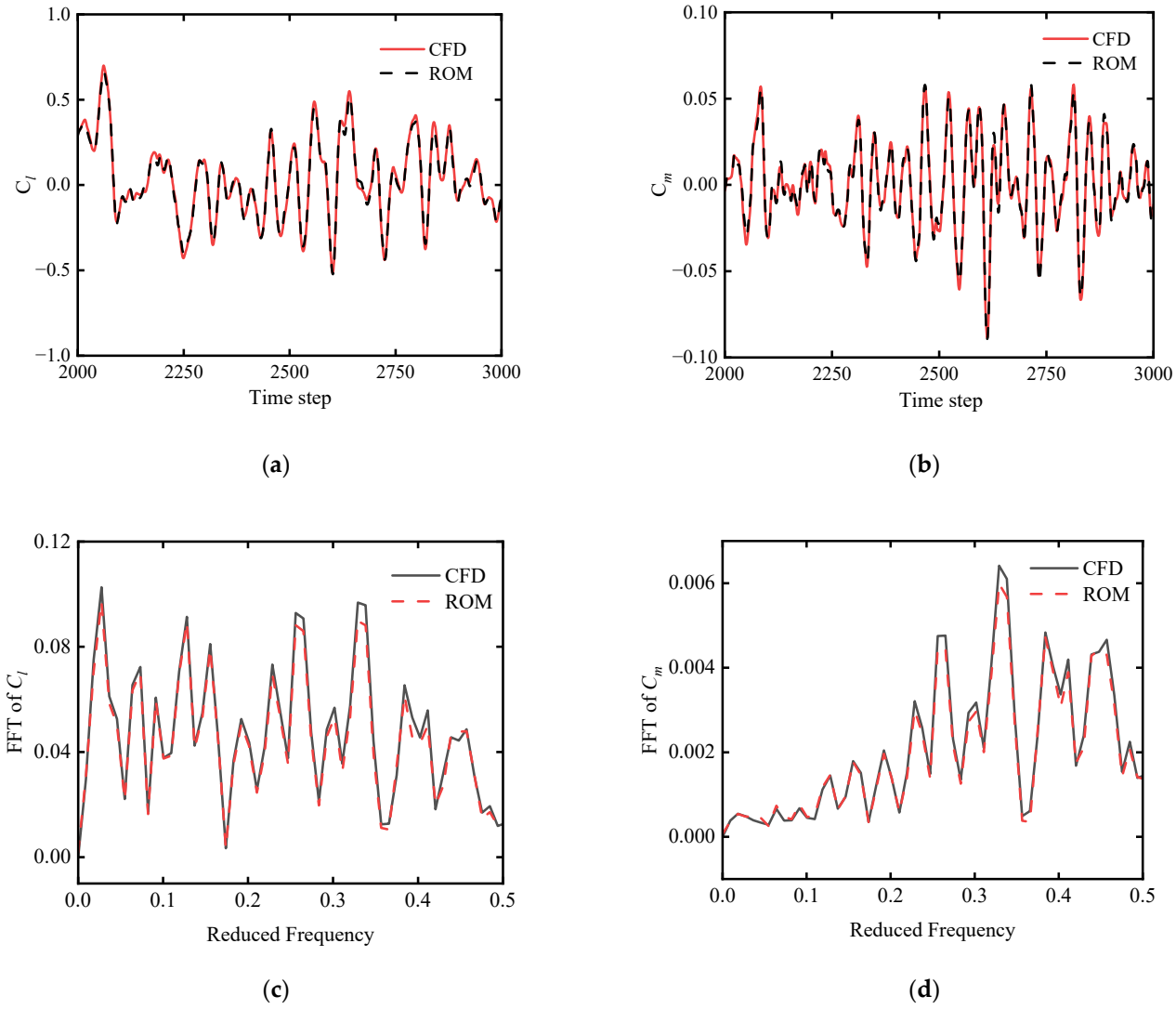
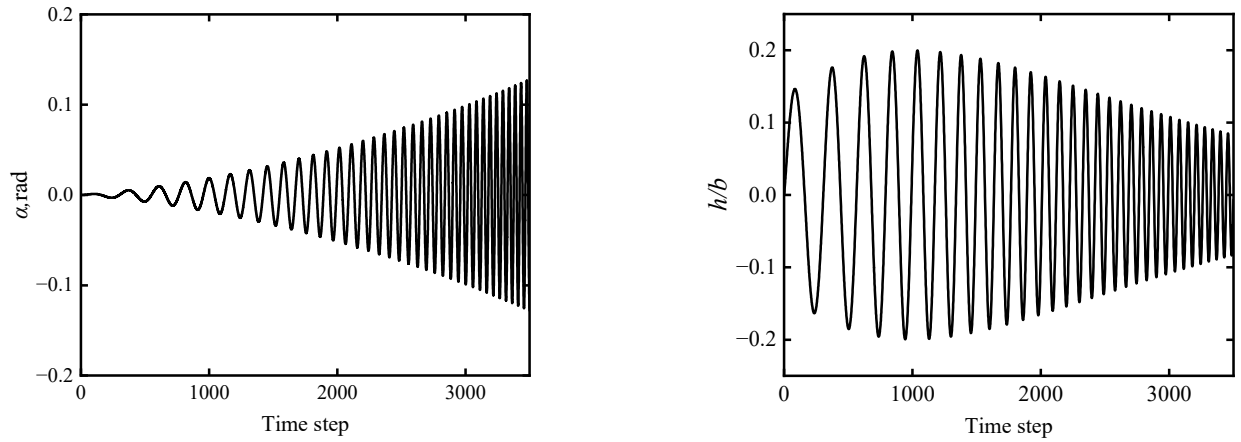


Figure 7. Comparison between CFD and ROM results under FWGN-based excitation, including time histories of the prediction interval, and the corresponding frequency-domain amplitude spectra as functions of reduced frequency: (**a**) Lift coefficient C_l, (**b**) moment coefficient C_m, (**c**) FFT of C_l, and (**d**) FFT of C_m.

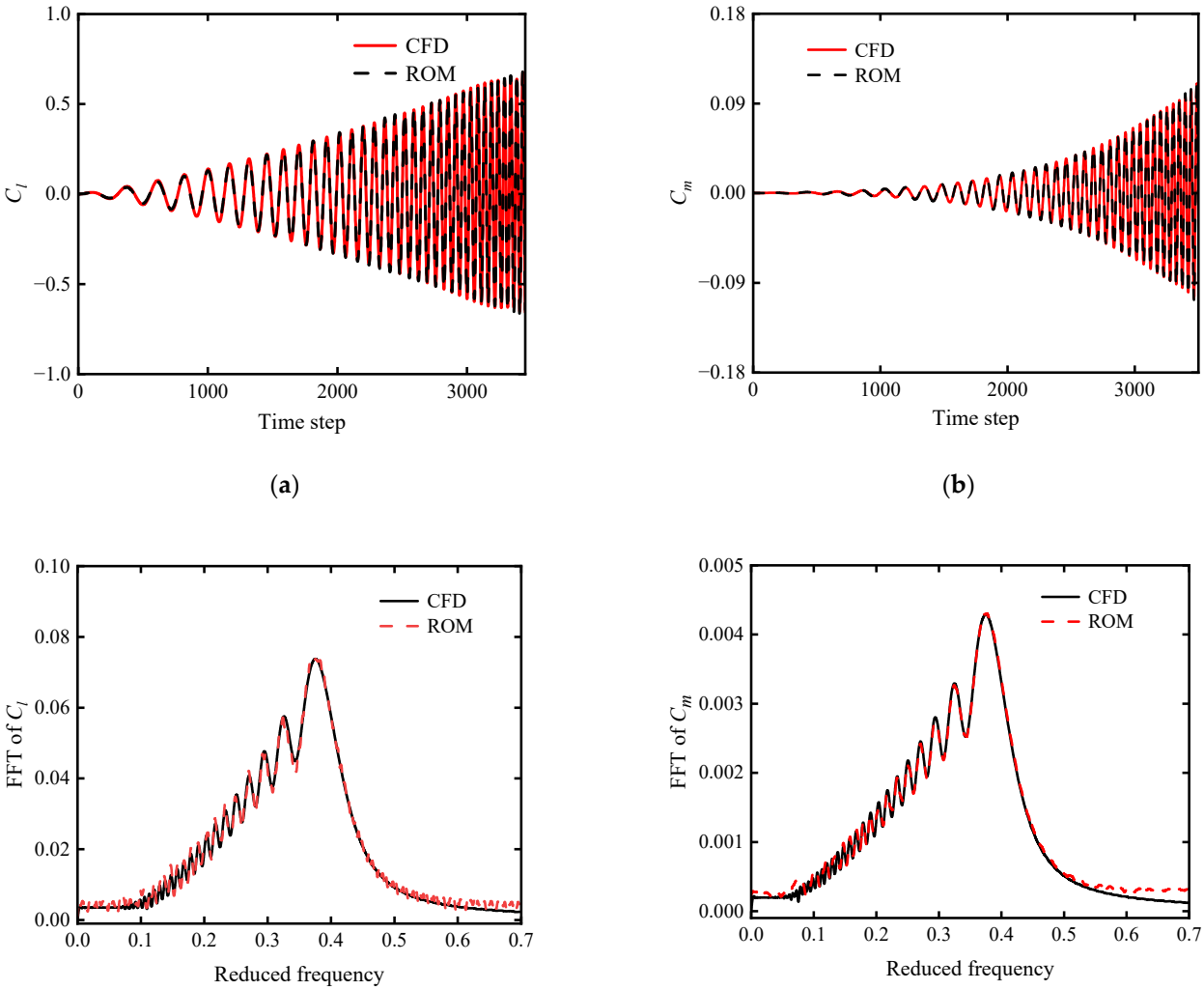
To evaluate the generalization capability of the developed ROM under varying motion amplitudes and frequency contents, two independent pitching and plunging frequency-sweep signals were generated, which were not included in the training dataset. Figure 8 illustrates these validation input signals, which maintain the same motion ranges as the training signals [42]. The ROM predictions are compared with the CFD results in both the time domain and the frequency domain (FFT) in Figures 9 and 10, respectively, demonstrating the model's performance across different motion conditions.

The time-domain comparisons indicate that the proposed ROM provides a close agreement with the CFD results for both independent pitching and independent plunging motions. The predicted lift and moment coefficients accurately reproduce the dominant unsteady aerodynamic responses over the entire simulation interval, including the overall amplitude evolution and phase characteristics.



(**a**) (**b**)

Figure 8. Independent input signals used to assess the predictive performance of the reduced-order model under pitching and plunging motions: (**a**) pitching motion; (**b**) plunging motion.



(**a**) (**b**)

(**c**) (**d**)

Figure 9. Comparative analysis of pitching motion input signal responses in the time and frequency domains: (**a**) lift coefficient C_l, (**b**) moment coefficient C_m, (**c**) FFT of C_l, and (**d**) FFT of C_m.

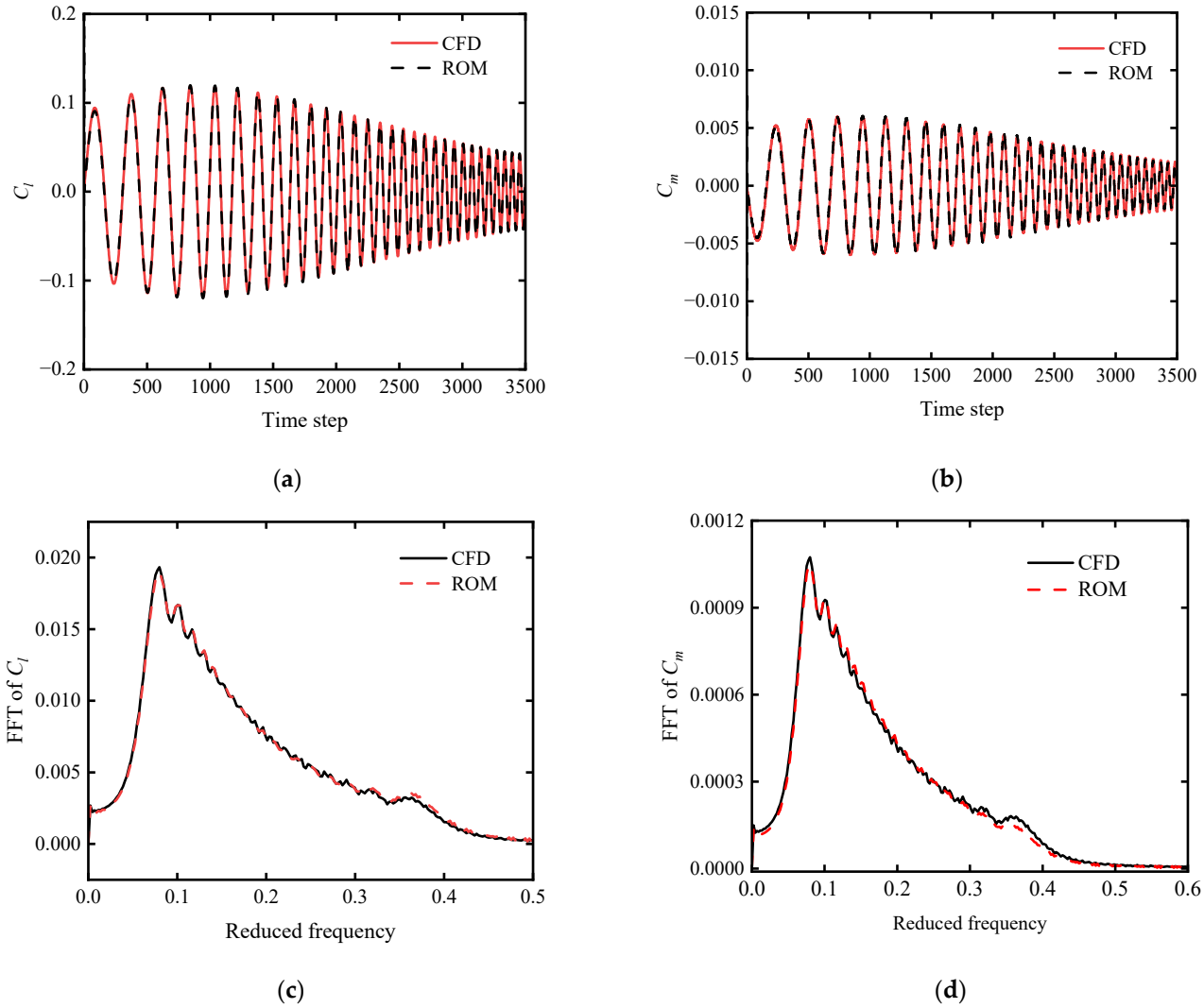


Figure 10. Comparative analysis of plunging motion input signal responses in the time and frequency domains: (**a**) Lift coefficient C_l, (**b**) moment coefficient C_m, (**c**) FFT of C_l, and (**d**) FFT of C_m.

The corresponding error statistics of the ROM predictions are reported in Table 2. For the independent pitching motion, the ROM achieves very small prediction errors for both the lift and moment coefficients. In particular, the RMSE values of C_l and C_m remain at low levels, while the corresponding R^2 values exceed 99%, indicating an excellent agreement with the CFD reference results and an accurate reproduction of the dominant unsteady aerodynamic responses. Similarly, for the independent plunging motion, the ROM predictions maintain low error levels across all metrics. The MAE and RMSE values for both aerodynamic coefficients are comparable to, or even smaller than, those obtained in the pitching case, and the R^2 values remain close to 99%. These results confirm the robustness of the proposed reduced-order model when applied to different types of independent motion inputs. Figure 11 shows the relative error between the ROM predictions and the CFD results as a function of reduced frequency, with the maximum error remaining below 5%. The achieved accuracy is therefore considered adequate for the coupled aeroelastic analysis.

The frequency-domain results further confirm the validity of the proposed ROM. In both motion cases, the ROM reproduces the dominant spectral content of the aerodynamic loads, with the main frequency peaks and their amplitudes showing consistency with the CFD results.

Table 2. Error results of ROM predictions under independent pitching and plunging motions.

Error Metric	Pithing Motion		Plunging Motion	
	C_L	C_M	C_l	C_M
MAE	0.006625	0.000112	0.00016	0.000186
MSE	0.009354	0.000001	0.000033	1.322×10^{-7}
RMSE	0.096714	0.000764	0.005712	0.000351
R^2	99.54%	99.15%	99.28%	99.03%

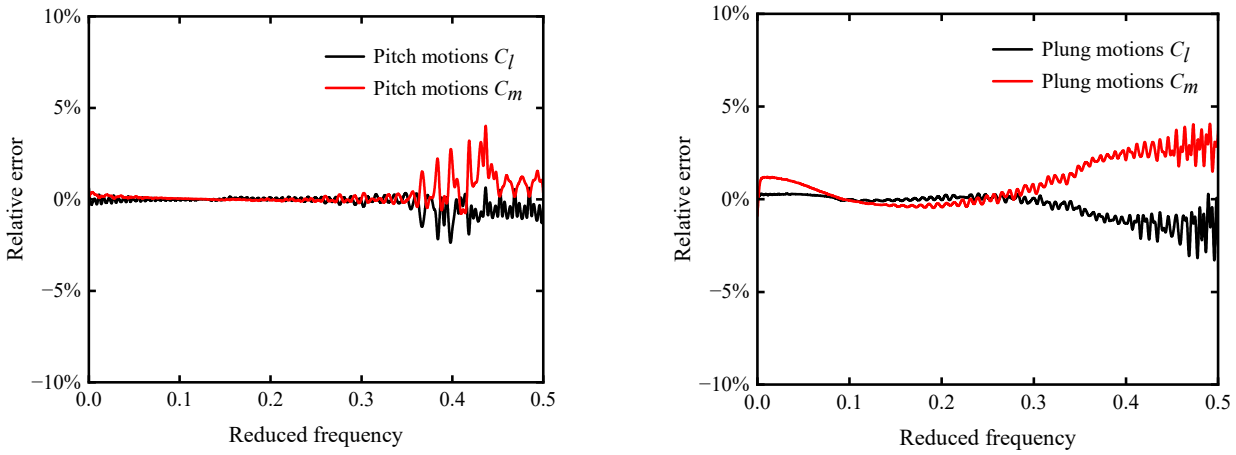


Figure 11. Relative Error of ROM for Pitching and Plunging Motions as a Function of Reduced Frequency: (**a**) Pitch Motion, (**b**) plunge Motion.

Minor deviations appear in the higher reduced-frequency range, where the ROM slightly under- or over-predicts secondary spectral components. These discrepancies are mainly attributed to the linear approximation inherent in the constructed state-space model and the truncation of higher-order nonlinear aerodynamic modes during the POD reduction process [37]. As a result, high-frequency nonlinear effects are not fully retained in the reduced-order representation. The present ROM is constructed by identifying the linear dynamical relationship of sectional unsteady aerodynamic loads over small time steps. Within the blade-element-based framework, the aerodynamic response at each blade section is evaluated largely in an independent manner and is primarily governed by the local effective angle of attack and inflow conditions [30]. Under these assumptions, the dominant sectional aerodynamics can be effectively represented using high-fidelity two-dimensional aerodynamic data while maintaining good computational efficiency.

5. Coupled ROM–CSD for Rotor Aeroelastic Analysis

In the present study, the rotor blade is modeled based on the blade element theory. The rotor blade is divided along the radial direction into a series of airfoil sections. Then, the unsteady aerodynamic loads at each blade section are evaluated independently based on the local flow conditions and motion states.

For each blade element, the sectional aerodynamic responses are determined by the local effective angle of attack and inflow velocity, which are influenced by the blade kinematics, including pitching and plunging motions. The aerodynamic forces and moments obtained at each section are then integrated along the blade span to reconstruct the total aerodynamic loads acting on the rotor blade.

Within this framework, the ROM developed for two-dimensional airfoil aerodynamics is employed to efficiently predict the unsteady sectional aerodynamic loads. By combining

the blade element theory with the validated ROM, the proposed approach provides an efficient and accurate aerodynamic modeling of the three-dimensional rotor while significantly reducing the computational cost compared to high-fidelity CFD simulations.

SA349/2 Forward Flight Test Case

A validation study is conducted based on the experimental data of the SA349/2 rotor under Flight Test 2 reported in Ref. [43]. In this case, the collective pitch is set to 6.93°, with the lateral cyclic pitch angles of 1.45°, longitudinal cyclic pitch angles of 1.04°, and the advance ratio is 0.14. The corresponding rotor blade parameters are adopted in the present Table 3. The geometric dimensions of the rotor blade as well as the sectional properties (e.g., density and stiffness distributions) are taken from Ref. [43].

Table 3. Basic parameters of the helicopter.

Parameters	Values
Airfoil	OA209
Number of Blades N_b	3
Operating Speed Ω/rpm	386
Rotor Radius R/m	5.25
Chord Length c/m	0.61
Rotor Thrust Coefficient C_T/σ	0.067

For the rotor blade, the ROM is established based on the blade element formulation. The periodic pitch motions of the blade sections are generated using FWGN, as illustrated in Figure 12. In the CFD simulations of the rotating rotor blade, the time step is selected as the time required for the rotor to rotate by 1°, ensuring sufficient temporal resolution of the unsteady aerodynamic responses. A total of 4321 time steps are generated, corresponding to 12 complete rotor revolutions. High-fidelity CFD simulations are then performed to obtain the sectional airfoil aerodynamic loads at different radial blade locations. Among the generated data, the first 3961 time steps (11 revolutions) are used for ROM training and system identification, while the remaining one revolution is reserved for validation of the predictive capability of the established ROM.

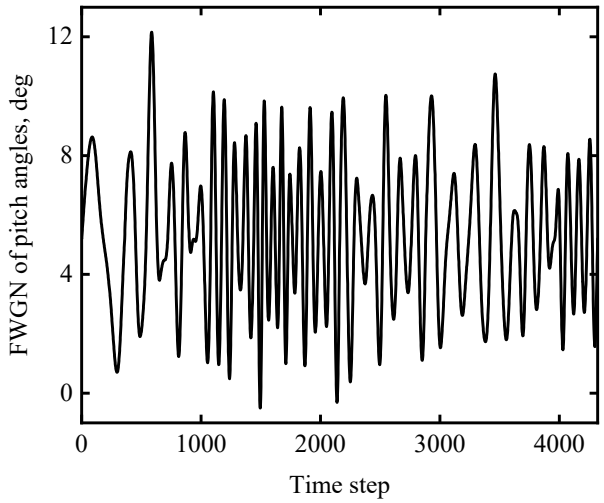


Figure 12. FWGN-generated sample input signals.

Figure 13 shows the energy ratios of the first ten POD modes (basis modes). The first mode is dominant, accounting for more than 97% of the total energy. The first two modes

represent more than 99% of the total energy, which indicates that the main flow features are well preserved by these modes.

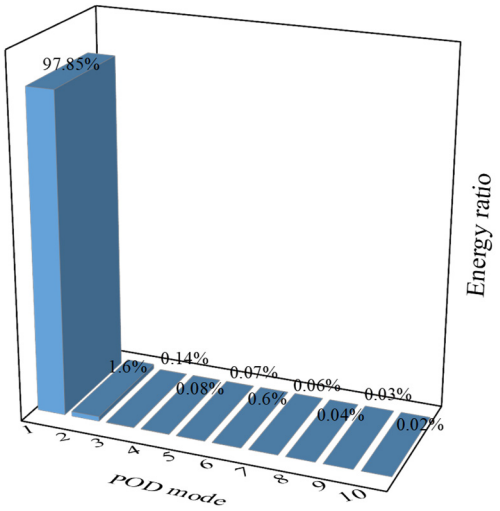


Figure 13. Energy ratios of first ten POD modes.

In addition to the numerical accuracy assessment, the physical significance of the dominant modes is briefly discussed. As shown in Figure 14 First four POD spatial modes of the rotor blade along the radial direction. The first four POD spatial modes exhibit spanwise distributions along the blade. The leading POD modes primarily capture the large-scale periodic aerodynamic response associated with blade pitching motion and represent the dominant energy-containing structures in the unsteady flow. Higher-order modes contribute to finer-scale flow variations and additional harmonic content. From the DMDc perspective, the identified modes correspond to the characteristic frequencies of the forced rotor/airfoil motion, indicating that the reduced-order model successfully captures the essential dynamic behavior of the unsteady aerodynamic system. This observed physical consistency further supports the reliability of the proposed POD–DMDc-based method for aeroelastic applications.

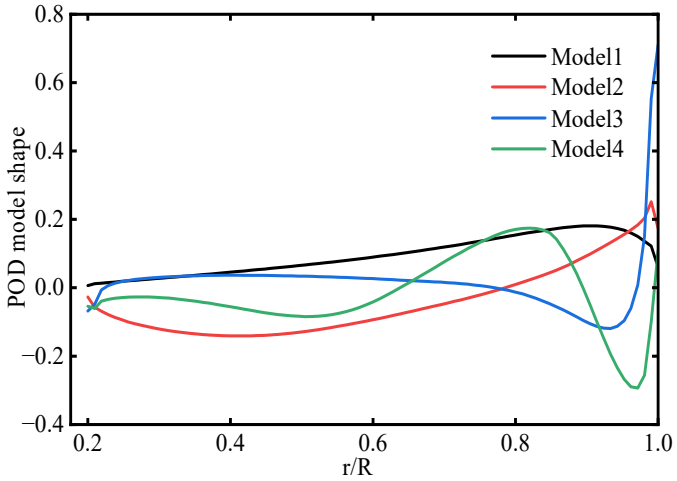


Figure 14. First four POD spatial modes of the rotor blade along the radial direction.

Figure 15 shows the comparison of the normal force coefficients at the 0.75 R and 0.88 R blade sections under forward-flight conditions. In the present study, a loosely coupled aeroelastic framework is adopted. For a three-bladed rotor, the aerodynamic solution is obtained over a 120° azimuthal rotation, and the complete rotor-disk aerodynamic loads are

reconstructed by phase-shifting and assembling the aerodynamic responses of individual blades. The reconstructed aerodynamic loads are subsequently transferred to the structural solver to compute the blade structural response over a full rotor revolution, completing one aeroelastic data-exchange cycle. This coupling strategy inevitably introduces discrepancies between the numerical predictions and the experimental measurements. The computational time is reduced from approximately 80 h on 96 CPU cores to a few minutes per simulation case, representing several orders of magnitude savings in computational cost.

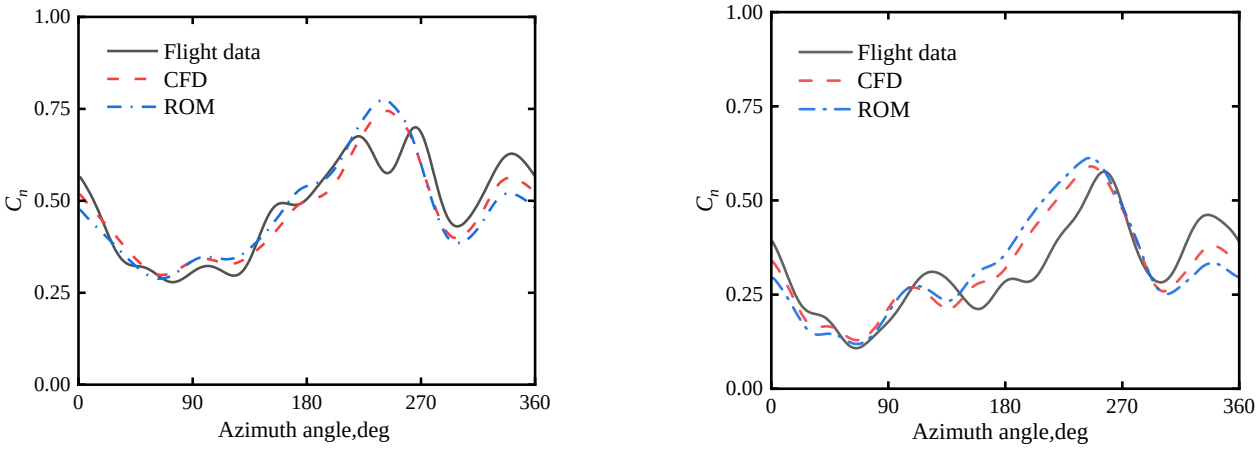


Figure 15. Comparison of normal force coefficients at different radial stations: (**a**) 0.75 R; (**b**) 0.88 R.

In addition, the natural frequencies of the SA349/2 rotor were calculated, including the three flap modes, the two lag modes, and the first torsional mode, which are denoted by F, L, and T, respectively, as shown in Figure 16. The results indicate that the CSD module exhibits slight discrepancies at low rotational speeds, whereas a good agreement is achieved at the nominal operating speed. Table 4 presents a comparison between the natural frequencies of the SA349/2 rotor obtained in the present study and the experimental data available in the literature. A reasonable level of agreement is observed between the two sets of results.

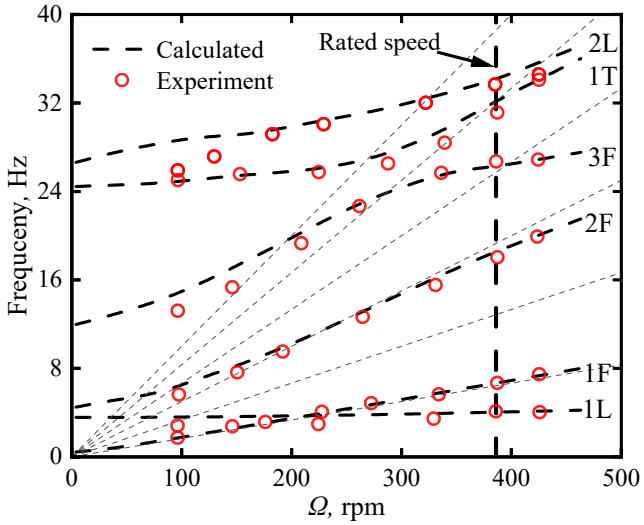


Figure 16. Frequency diagram of the SA349/2 rotor blade.

Table 4. Calculation results of natural frequencies of SA349/2 rotor.

Mode	Experiment [43]	Calculated	Relative Error/%
1F	6.6765	6.6761	0.005%
2F	18.0945	18.5729	2.64%
3F	26.8152	26.248	2.11%
1L	3.91808	4.0446	3.23%
2L	33.6963	34.097	1.19%
1T	31.243	32.180	2.98%

As shown in Figure 17, the calculated data shown in the figure are obtained from the ROM–CSD coupled model. The flight-test data presented in the figure are taken from Ref. [43], while the CAMRAD computational results are taken from Ref. [44]. The observed discrepancies may be attributed to the simplified aerodynamic modeling and the absence of high-frequency unsteady effects in the CSD formulation. In particular, when the blade rotates into the retreating side, larger deviations are observed at the outboard blade sections, where strong nonlinear aerodynamic effects associated with dynamic stall are not fully captured by the present modeling framework. Overall, the coupled CSD predictions show good agreement with the experimental data in terms of both phase and amplitude, demonstrating the capability of the proposed model to capture the unsteady bending loads of the SA349/2 rotor.

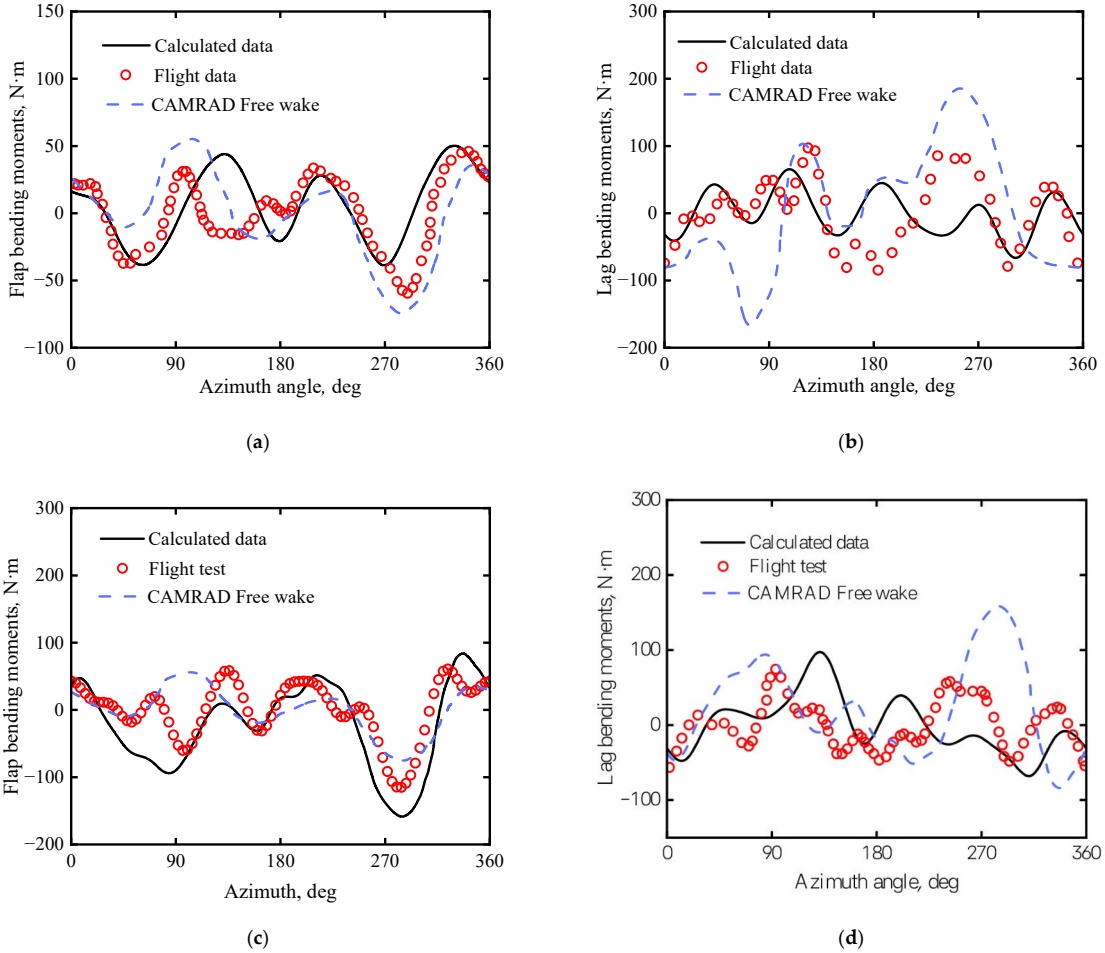


Figure 17. Comparison of flap and lag bending moments at different radial stations: (**a**) Flap bending moment at 0.54 R, (**b**) Lag bending moment at 0.54 R, (**c**) Flap bending moment at 0.80 R, (**d**) Lag bending moment at 0.80 R.

Within the blade-element framework, the model may not fully capture certain physical mechanisms in regions where three-dimensional flow features become pronounced, such as tip-loss effects, root interactions, and strong spanwise flows under highly unsteady conditions. In addition, under the loosely coupled strategy, the phase lag introduced by the finite information exchange frequency between the aerodynamic and structural solvers may weaken some transient aerodynamic features. For the SA349/2 rotor, the presence of the hydraulic damper also affects the measured structural loads, particularly in the lead–lag response (as shown in Figure 17, the flap bending moment exhibits better agreement than the lag component). However, the publicly available experimental data [43] provide only an equivalent dissipation coefficient, which limits the ability of the present model to fully reconstruct the detailed damper dynamics. This modeling uncertainty may also contribute to some of the observed discrepancies. Despite the above factors, the coupled ROM–CSD predictions still show overall good agreement with the experimental measurements and the CAMRAD [44] results, indicating that the proposed approach is able to achieve a reasonable balance between computational efficiency and predictive accuracy for the operating conditions considered in this study and demonstrates promising potential for engineering applications.

6. Conclusions

In this paper, a ROM model for unsteady aerodynamic load prediction and aeroelastic analysis is developed and validated. The study progresses from two-dimensional airfoil motions to three-dimensional rotor blade applications, and further to a coupled ROM–CSD simulation of a full rotor system. The main conclusions are summarized as follows:

1. A ROM for unsteady aerodynamics is first established based on two-dimensional airfoil cases under independent pitching and plunging motions. Time-domain and frequency-domain comparisons demonstrate that the ROM accurately reproduces the dominant unsteady aerodynamic responses obtained from CFD simulations, including both amplitude evolution and phase characteristics. Quantitative error metrics, including MAE, MSE, RMSE, and R^2, indicate high prediction accuracy for both lift and moment coefficients. Specifically, the coefficient of determination exceeds 99.03% in cases, confirming the robustness and reliability of the proposed ROM under different motion excitations.
2. The ROM model is successfully extended to three-dimensional rotor blade applications using sectional modeling. Broadband periodic excitations generated by frequency-weighted Gaussian noise (FWGN) ensure sufficient excitation of the aerodynamic system. Comparisons of sectional normal force coefficients at multiple radial stations show good agreement among ROM predictions, CFD results, and available flight test data, confirming the robustness of the reduced-order model in forward flight conditions.
3. A loosely coupled aeroelastic strategy is adopted to integrate the ROM with a CSD solver. The natural frequencies of the SA349/2 rotor blade, including flap, lag, and torsional modes, are accurately predicted and show close agreement with flight test results and experimental data, with the maximum relative error of the predicted natural frequencies remaining below 3.5%. These results confirm the reliability of the structural modeling and the correctness of the modal characteristics used in the aeroelastic simulations.
4. Coupled ROM–CSD simulations are performed to predict the flap and lag bending moments at different radial locations along the blade. The predicted bending moments show good agreement with experimental measurements in terms of both amplitude and phase. The results indicate that unsteady aerodynamic loads and structural

responses become more pronounced toward the outboard blade regions. It is noted that relatively larger discrepancies are observed at the outer blade sections when the blade rotates into the retreating side, which may be attributed to the strong nonlinear aerodynamic effects associated with dynamic stall and reverse-flow phenomena in the retreating-blade region, leading to increased modeling errors in the structural response prediction.

Although CFD-based approaches have significantly improved aerodynamic prediction accuracy compared with traditional reduced-order models, efficiently incorporating high-fidelity aerodynamic information into aeroelastic analysis and load prediction still requires further methodological development. To address this issue, the present study constructs a reduced-order model by identifying the linear dynamical relationship of sectional unsteady aerodynamic loads over small time steps. Within the framework of blade element theory, the aerodynamic response of each blade section is evaluated in an approximately independent manner. Under these assumptions, the dominant sectional aerodynamic characteristics can be effectively represented using high-fidelity two-dimensional aerodynamic data while maintaining good computational efficiency. This strategy aims to retain, to the greatest extent possible, the unsteady aerodynamic physics resolved by CFD while substantially reducing the computational burden in subsequent aeroelastic load prediction and potential optimization applications.

Nevertheless, further improvements remain possible. Future work will focus on extending the present method to higher advance ratios and more complex maneuvering flight conditions, where stronger nonlinear aerodynamic effects may arise (particularly near the blade tip, root region, or under strongly three-dimensional unsteady flow conditions). In addition, future developments of the aerodynamic modeling will incorporate three-dimensional aerodynamic effects to further improve prediction accuracy and broaden the applicability of the proposed method.

Author Contributions: Conceptualization, N.L. and Z.Y.; methodology, N.L. and Z.Y.; software, N.L.; validation, N.L.; resources, N.L.; data curation, N.L.; writing—original draft preparation, N.L.; writing—review and editing, Z.Y.; visualization, Z.Y.; supervision, W.Y.; project administration, Z.Y.; funding acquisition, Z.Y. All authors have read and agreed to the published version of the manuscript.

Funding: This research was supported by the Special Fund of National Key Laboratory of Helicopter Aeromechanics of China (NO. ZAG25006-04).

Data Availability Statement: Data are contained within the article.

Conflicts of Interest: The authors declare no conflicts of interest.

References

1. Sun, Y.; Shi, Y.; Xu, G. Application of High-Order WENO Scheme in the CFD/FW–H Method to Predict Helicopter Rotor Blade–Vortex Interaction Tonal Noise. *Aerospace* **2022**, *9*, 196. [CrossRef]
2. Ajaj, R.M.; Omar, F.K.; Darabseh, T.T.; Cooper, J. Flutter of Telescopic Span Morphing Wings. *Int. J. Struct. Stab. Dyn.* **2019**, *19*, 1950061. [CrossRef]
3. Lim, I.G.; Lee, I. Aeroelastic analysis of bearingless rotors using large deflection beam theory. *AIAA J.* **2007**, *45*, 599–606. [CrossRef]
4. Hodges, D.H. *Nonlinear Composite Beam Theory*; Progress in Astronautics and Aeronautics; American Institute of Aeronautics and Astronautics: Reston, VA, USA, 2006; Volume 213.
5. Cesnik, C.E.S.; Hodges, D.H. VABS: A New Concept for Composite Rotor Blade Cross-Sectional Modeling. *J. Am. Helicopter Soc.* **1997**, *42*, 27. [CrossRef]
6. Shen, J.W.; Chopra, I. Swashplateless helicopter rotor with trailing-edge flaps. *J. Aircr.* **2015**, *41*, 208–214. [CrossRef]
7. Shang, L.; Xia, P.; Lin, Z.C. Geometrically exact aeroelastic stability analysis of helicopter composite rotor blades in forward flight. *Aerosp. Sci. Technol.* **2024**, *144*, 108818. [CrossRef]

8. Vindigni, C.R.; Mantegna, G.; Esposito, A.; Orlando, C.; Alaimo, A. An aeroelastic beam finite element for time domain preliminary aeroelastic analysis. *Mech. Adv. Mater. Struct.* **2023**, *30*, 1064–1072. [CrossRef]
9. Wang, J.C.; Tan, J.F.; Li, J.B.; Xu, M. Investigation of autorotating rotor aerodynamic characteristics based on free wake method. *Chin. J. Aeronaut.* **2015**, *36*, 3540–3548. (In Chinese)
10. Dowell, E. Reduced-order modeling: A personal journey. *Nonlinear Dyn.* **2023**, *111*, 9699–9720. [CrossRef]
11. Peters, D.A.; Hsieh, M.C.A.; Torrero, A. A State-Space Airloads Theory for Flexible Airfoils. *J. Am. Helicopter Soc.* **2007**, *52*, 329–342. [CrossRef]
12. Tung, C.; Caradonna, F.X.; Johnson, W.R. The prediction of transonic flows on an advancing rotor. *J. Am. Helicopter Soc.* **1986**, *31*, 4–9. [CrossRef]
13. Kim, K.C.; Desopper, A.; Chopra, I. Blade Response calculations using three-dimensional aerodynamic modeling. *J. Am. Helicopter Soc.* **1991**, *36*, 68–77. [CrossRef]
14. Mill, M. Coupled Fluid-Structure Simulations of Helicopter Rotors. Ph.D. Thesis, The Pennsylvania State University, University Park, PA, USA, 2006.
15. Datta, A.; Chopra, I. Prediction of the UH-60A main rotor structural loads using computational fluid dynamics/comprehensive analysis coupling. *J. Am. Helicopter Soc.* **2008**, *53*, 351–365. [CrossRef]
16. Datta, A.; Sitaraman, J.; Chopra, I.; Baeder, J.D. CFD/CSD Prediction of Rotor Vibratory Loads in High-Speed Flight. *J. Aircr.* **2006**, *43*, 1698–1709. [CrossRef]
17. Smith, M.J.; Lim, J.W.; van der Wall, B.G.; Baeder, J.D.; Biedron, R.T.; Boyd, D.D., Jr.; Jayaraman, B.; Jung, S.N.; Min, B.-Y. An assessment of CFD/CSD prediction state-of-the-art using the HART II international workshop data. In *68th Annual Forum & Technology Display*; AHS International: Fort Worth, TX, USA, 2012.
18. Fukami, K.; Araki, R. Information-Theoretic Machine Learning for Time-Varying Mode Decomposition of Separated Aerodynamic Flows. *AIAA J.* **2026**, *64*, 605–613. [CrossRef]
19. Schmid, P.J. Dynamic Mode Decomposition of Numerical and Experimental Data. *J. Fluid Mech.* **2010**, *656*, 5–28. [CrossRef]
20. Lumley, J. *Stochastic Tools in Turbulence*; Academic Press: New York, NY, USA, 1970; pp. 114–116.
21. Lumley, J.L. The structure of inhomogeneous turbulence. In *Atmospheric Turbulence and Wave Propagation*; Yaglom, A.M., Tatarski, V.I., Eds.; Atmospheric Turbulence and Wave Propagation: Moscow, Russia, 1967; pp. 166–178.
22. Romanowski, M. Reduced order unsteady aerodynamic and aeroelastic models using Karhunen-Loeve eigenmodes. In *6th Symposium on Multidisciplinary Analysis and Optimization*; American Institute of Aeronautics and Astronautics: Bellevue, WA, USA, 1996; p. 3981.
23. Hall, K.C.; Thomas, J.P.; Dowell, E.H. Proper orthogonal decomposition technique for transonic unsteady aerodynamic flows. *AIAA J.* **2000**, *38*, 1853–1862. [CrossRef]
24. Kou, J.; Zhang, W. Dynamic mode decomposition with exogenous input for data-driven modeling of unsteady flows. *Phys. Fluids* **2019**, *31*, 057106. [CrossRef]
25. Shi, Z.; Gao, C.; Zhang, W. Data-knowledge-driven dynamic stall modeling guided by stall patterns and semi-empirical model. *Phys. Fluids* **2025**, *37*, 045106. [CrossRef]
26. Proctor, J.L.; Brunton, S.L.; Kutz, J.N. Dynamic mode decomposition with control. *SIAM J. Appl. Dyn. Syst.* **2014**, *15*, 1101–1109. [CrossRef]
27. Fonzi, N.; Brunton, S.L.; Fasel, U. Data-driven nonlinear aeroelastic models of morphing wings for control. *Proc. R. Soc. A Math. Phys. Eng. Sci.* **2020**, *476*, 20200079. [CrossRef]
28. Lin, Y.; Yang, W.; Wang, H.; Wang, F.; Hu, J.; Yao, J. Application of Proper Orthogonal Decomposition in Spatiotemporal Characterization and Reduced-Order Modeling of Rotor–Stator Interaction Flow Field. *Aerospace* **2025**, *12*, 365. [CrossRef]
29. Yao, X.; Huang, R.; Hu, H.; Liu, H. Transonic aerodynamic–structural coupling characteristics predicted by nonlinear data-driven modeling approach. *AIAA J.* **2024**, *62*, 1159–1178. [CrossRef]
30. Fonzi, N.; Brunton, S.L.; Fasel, U. Data-Driven Modeling for Transonic Aeroelastic Analysis. *J. Aircr.* **2024**, *61*, 625–637. [CrossRef]
31. Baum, J.D.; Luo, H.; Mestreau, E.L.; Sharov, D.; Löhner, R.; Pelessone, D.; Charman, C. Recent developments of a coupled CFD/CSD methodology. In *International Conference on Computational Science*; Springer: Berlin/Heidelberg, Germany, 2001; pp. 1087–1097.
32. Wang, H.; Zhang, X.; Zhao, Q.; Ma, L.; Bian, W.; Liu, S.; Gong, Y. Aeroelastic characteristics and vibration reduction method of NTBT rotor with TEF technology. *Chin. J. Aeronaut.* **2026**, *39*, 268–287. [CrossRef]
33. Gedda, G.; Ferrero, A.; Masseni, F.; Mariani, M.; Pastrone, D. Reduced-Order Modeling and Active Subspace to Support Shape Optimization of Centrifugal Pumps. *Aerospace* **2025**, *12*, 1007. [CrossRef]
34. Gu, X.; Dong, L.; Li, T.; Yang, W. A Study on Influence of Flapping Dynamic Characteristics on Vibration Control of Active Rotor with Trailing-Edge Flaps. *Aerospace* **2023**, *10*, 776. [CrossRef]
35. Mcalister, K.W.; Pucci, S.L.; Carr, L.W. *An Experimental Study of Dynamic Stall on Advanced Airfoil Sections, Volume 2. Pressure and Force Data: NASA-TM-84245*; NASA Ames Research Center: Moffett Field, CA, USA, 1982.

36. Silva, W.A. Simultaneous Excitation of Multiple-Input/Multiple-Out-put CFD-Based Unsteady Aerodynamic Systems. *J. Aircr.* **2008**, *45*, 1267–1274. [CrossRef]
37. Yao, X.; Huang, R.; Hu, H. Data-driven modeling of transonic unsteady flows and efficient analysis of fluid-structure stability. *J. Fluids Struct.* **2022**, *111*, 103549. [CrossRef]
38. Goto, S.; Nakai, K.; Kanda, N.; Iwasaki, Y.; Nonomura, T.; Asai, K. Data-Driven Reconstruction of Velocity Field Around Airfoil Using Unsteady Surface Pressure Measurement. In *AIAA Scitech 2022 Forum*; AIAA Paper: Orlando, FL, USA, 2022; p. 0139.
39. Yang, C.; Liu, X.Y.; Wu, Z.G. Unsteady aerodynamic modeling based on POD-observer method. *Sci. China Technol. Sci.* **2010**, *53*, 2032–2037. [CrossRef]
40. Kou, J.; Zhang, W.; Ye, Z. Dynamic nonlinear aerodynamics modeling method based on layered model. *Acta Aeronaut. Astronaut. Sin.* **2015**, *36*, 3785–3797.
41. Kou, J.; Zhang, W.; Yin, M. Novel Wiener models with a time-delayed nonlinear block and their identification. *Nonlinear Dyn.* **2016**, *85*, 2389–2404. [CrossRef]
42. Kou, J.; Zhang, W. Layered reduced-order models for nonlinear aerodynamics and aeroelasticity. *J. Fluids Struct.* **2017**, *68*, 174–193. [CrossRef]
43. Heffernan, R.M.; Gaubert, M. *Structural and Aerodynamic Loads and Performance Measurements of anSA349/2 Helicopter with an Advanced Geometry Rotor: NASA-TM-88370*; NASA: Washington, DC, USA, 1986.
44. Yamauchi, G.K.; Heffernan, R.M.; Gaubert, M. Correlation of sa349/2 helicopter flight test data with a comprehensive rotorcraft model. *J. Am. Helicopter Soc.* **1987**, *33*, 31–42. [CrossRef]

Disclaimer/Publisher's Note: The statements, opinions and data contained in all publications are solely those of the individual author(s) and contributor(s) and not of MDPI and/or the editor(s). MDPI and/or the editor(s) disclaim responsibility for any injury to people or property resulting from any ideas, methods, instructions or products referred to in the content.